Comparison of breaking models in envelope-based surface gravity wave evolution equations

Yuxuan Liu [1,*] D. Eeltink [1,2] Tianning Tang [1] D. Barratt,[1] Ye Li [3]
T. A. A. Adcock [1] and T. S. van den Bremer [1,4]

[1]*Department of Engineering Science, University of Oxford, Oxford OX1 3PJ, United Kingdom*
[2]*Department of Mechanical Engineering, Massachusetts Institute of Technology,
Cambridge, Massachusetts 02139-4307, USA*
[3]*Multiple Function Towing Tank Laboratory, State Key Laboratory of Ocean Engineering,
School of Naval Architecture, Ocean and Civil Engineering, Shanghai Jiao Tong University,
Shangai 200240, China*
[4]*Faculty of Civil Engineering and Geosciences, Delft University of Technology,
2628 CD Delft, The Netherlands*

Wave breaking is the main mechanism that dissipates energy from ocean waves by wind. Its effects on the frequency spectrum cause a downshift of the spectral peak and dissipation of the total energy of the spectrum. Various reduced-form wave breaking models have been developed to capture wave breaking in envelope-based wave evolution equations for perturbed plane-wave systems, but their applicability to waves with a continuous spectrum has not been examined. In this paper we perform modified nonlinear Schrödinger equation simulations to study four existing wave breaking models and compare the results with new experimental data for breaking unidirectional wave groups. We first compare the different wave breaking models for perturbed plane-wave simulations and then examine their potential extension to waves with a continuous spectrum. We find that most existing models are able to model breaking in perturbed plane waves, but none produce the correct spectral dissipation for focused wave groups. We propose a modification to the breaking model by Kato and Oikawa [J. Phys. Soc. Jpn. **64**, 4660 (1995)] in order to model breaking in focused wave groups. The modified model incorporates both a breaking criterion, which activates and deactivates the dissipation term proposed by Kato and Oikawa, and a heuristic spectral weighting function that is obtained by fitting to experimental data. The modified model also predicts breaking in perturbed plane waves well.

I. INTRODUCTION

Surface gravity wave breaking is a familiar phenomenon to those observing the ocean [1], yet a good understanding capturing the fundamental physics of wave breaking has proved difficult for scientists and engineers. Understanding breaking is important for multiple reasons, including energy balance in the ocean [2], ocean mixing, air-sea interactions [3,4], influencing short-term wave statistics [5], and loading on maritime structures [6].

---

*Corresponding author: yuxuan.liu@eng.ox.ac.uk

Understanding the problem of wave breaking on a wave-by-wave basis (as opposed to a phased-averaged sea-state analysis) can be crudely broken down into understanding when waves break and then understanding the subsequent evolution. Wave breaking criteria typically use the wave steepness, wave speed, and water depth to provide a threshold above which waves would break. The postbreaking behavior is a complex multiscale process. Both parts of the problem are active areas of research.

Another problem in ocean wave physics is modeling the evolution of nonbreaking waves, which is considered a (weakly) nonlinear process. A widely used model for deep-water waves is the nonlinear Schrödinger (NLS) equation and its higher-order, or "modified" (MNLS) [7] variants (see [8] for an account of how these have developed). They model the evolution of a wave envelope, which must be multiplied by a carrier wave to obtain the free surface elevation. Due to their underlying assumptions, the validity of these models is restricted to the spectra of limited bandwidth. Generally, these equations can predict the evolution of ocean waves well, although prediction of the largest waves remains challenging due to the nonlinear physics driving a local broadening of the spectrum [9]. The great benefit of these equations is that they are computationally fast and thus are ideal for performing long-duration random simulations. However, in any random simulation there will be some wave breaking which is not captured in the basic MNLS equations. Thus it is necessary to modify the standard equations in order to capture this process by adding a reduced-form or data-driven breaking term (e.g., [10]). Such a model can never be perfect—wave breaking is highly complex, turbulent, and three-dimensional—but even if the model is imperfect locally, it is important that the dominant spectral changes are quantitatively captured. This is the topic of the present paper.

A number of existing breaking models can be added to the MNLS equation as a dissipation term D (cf. Ref. [3], discussed in detail in Sec. 2.2). We will examine four. Trulsen and Dysthe (1990) [11] developed a damping term that switches on when the amplitude of the waves reaches above a threshold. Kato and Oikawa (1995) [12] modified the return-current term in the MNLS equation to capture breaking, with breaking essentially turning on when the spectrum broadens. Similarly, applying a selective Laplacian term [13] dampens frequency components above a certain threshold. Alternatively, the energy balance equation can be used to derive a breaking module from first principles [14,15].

Our aim is to examine how well these four reduced-form breaking models capture wave breaking and subsequent (nonlinear) wave evolution in different scenarios. We begin by examining perturbed plane wave—this scenario has been studied extensively in the literature [16,17], and the discrete nature of the problem makes an investigation of the nonlinear energy transfers straightforward, resulting in a form of Fermi–Pasta–Ulam–Tsingu (FPUT) recurrence [18,19] in the absence of breaking. Classically, perturbed plane waves have been used to study the impact of breaking [15,20]. However, ocean waves are formed by a continuous spectrum, so we secondly we consider breaking of focused wave groups, which can be used to model the expected shape of an extreme event in a random sea.

In this study first we review four existing breaking models for plane waves and investigate their ability to predict postbreaking wave fields for focused wave groups. To do so we make a direct comparison between numerical simulations of the MNLS equation with an added reduced-form breaking and experimental observations. Secondly, we examine how existing breaking models may be modified. While the breaking signature is clear for nonlinearly steepening plane waves (the permanent frequency downshift), our study aims at better understanding wave breaking for focused wave groups. While it is clearly not possible to capture the detailed physics of wave breaking in a simple envelope-based model, a correct prediction of the postbreaking wave field indicates the most important physical features are captured.

Wave breaking is a three-dimensional (3D) phenomena in nature. This is true both for breaking inception and for the subsequent physical processes [21]. However, two-dimensional (2D) simulations are routinely used, and our goal here is to understand how well the real 3D process is captured

in such 2D models where we are not explicitly modeling such 3D physics as vortex filaments, crescent wave, or directionally spread waves.

This paper is organized as follows. Section II introduces our theoretical and experimental methodology. Section III examines the performance of four existing reduced-form breaking models for the canonical case of perturbed plane waves. Section IV then examines the performance of these four models for focused wave groups by comparing to experiments we have performed. Section V examines how the existing models can be optimized or modified, and Sec. VI concludes.

II. THEORETICAL AND EXPERIMENTAL METHODOLOGY

For our wave simulations, we use the modified nonlinear Schrödinger equation proposed by [22]. This model solves the linear part of the envelope evolution exactly and approximates the effects of nonlinearity. Four different existing reduced-form breaking models are then added in turn as a dissipation term to the MNLS equation.

A. Envelope-based evolution equation

The harmonic expansions for the velocity potential ϕ and the surface elevation η can be written as

$$\phi = \bar{\phi} + \tfrac{1}{2}\big(Ae^{i(k_0x-\omega_0t)+k_0z} + A_2e^{2i(k_0x-\omega_0t)+2k_0z} + \cdots + \text{c.c.}\big), \tag{1}$$

$$\eta = \bar{\eta} + \tfrac{1}{2}\big(Be^{i(k_0x-\omega_0t)} + B_2e^{2i(k_0x-\omega_0t)} + \cdots + \text{c.c.}\big), \tag{2}$$

where c.c. denotes the complex conjugate, k_0 and ω_0 are the wave number and angular frequency of the carrier wave, $A(x,z,t)$ and $B(x,t)$ are complex envelopes, and $\bar{\phi}$ and $\bar{\eta}$ are the mean-flow potential and the wave-averaged free surface, respectively. The envelope $B(x,t)$ is described by the MNLS equation [22] (given here in two dimensions or for unidirectional wave propagation):

$$\frac{\partial B}{\partial t} + L(\partial x)B + \frac{i\omega_0k_0^2}{2}|B|^2B + \frac{3\omega_0k_0}{2}|B|^2\frac{\partial B}{\partial x} + \frac{\omega_0k_0}{4}B^2\frac{\partial B^*}{\partial x} + ik_0\frac{\partial\bar{\phi}}{\partial x}B + D = 0, \tag{3}$$

$$\frac{\partial\bar{\phi}}{\partial z} = \frac{\omega_0}{2}\frac{\partial}{\partial x}|B|^2 \quad \text{at } z = 0, \tag{4}$$

$$\nabla^2\bar{\phi} = 0 \quad \text{for } -\infty < z < 0, \tag{5}$$

$$\frac{\partial\bar{\phi}}{\partial z} = 0 \quad \text{for } z \to -\infty, \tag{6}$$

where B^* denotes the complex conjugate of B, and D is the dissipation term that will be used to incorporate the reduced-form breaking models into the MNLS. In Fourier wave-number space, the linear operator $L(\partial x)$ can be written as [22]

$$\frac{\partial\hat{B}}{\partial t} + i[\omega(k_0 + \lambda) - \omega_0]\hat{B} = 0, \tag{7}$$

where λ is the modulation wave number.

We solve (3) using a spectral method in space and a fourth-order Runge–Kutta method to advance in time. The complex envelope $B(x, t = 0)$ is required as an initial condition for the solver. We either compute the envelope directly or reconstruct it from the linearized Hilbert transform of the surface elevation profile.

The first-order surface elevation is obtained by shifting the complex envelope to the carrier frequency and taking the real part:

$$\eta_1 = \text{Re}\big(Be^{i(k_0x-\omega_0t)}\big). \tag{8}$$

To achieve better agreement with experimentally measured surface elevation η, second-order subharmonic η_{2-}, second-order superharmonic η_{2+}, and third-order superharmonic η_3 bound waves are reconstructed according to [23,24]

$$\eta_{2-} = \text{Re}\left(\frac{1}{2\omega_0}\frac{\partial\bar{\phi}}{\partial x} - \frac{1}{16k_0}\frac{\partial^2|B|^2}{\partial x^2}\right), \tag{9}$$

$$\eta_{2+} = \text{Re}\left(\left[\frac{k_0 B^2}{2} - \frac{iB}{2}\frac{\partial B}{\partial x}\right]e^{2i(k_0 x - \omega_0 t)}\right), \tag{10}$$

$$\eta_3 = \text{Re}\left(\frac{3}{8}k_0^2 B^2 e^{3i(k_0 x - \omega_0 t)}\right), \tag{11}$$

and we compute $\eta = \eta_1 + \eta_{2-} + \eta_{2+} + \eta_3$.

We use a one-dimensional (1D) uniform mesh, and the 1D computational domain is configured to ensure that the wave group does not interact with the end of the domain or collide with itself during dispersion. The length of the computing domain spans $[-100\lambda_0, 100\lambda_0]$ in the wave propagation direction, and the resolution is $0.04\lambda_0$, where λ_0 is the carrier wavelength. The left- and right-hand sides of the domain are periodic boundaries.

B. Four reduced-form breaking models

We will investigate the following four existing reduced-form breaking models: the damping term introduced by Trulsen and Dysthe (1990) [11] (TD90 hereinafter); the modified return-current term introduced by Kato and Oikawa (1995) [12] (KO95 hereinafter); the selective Laplacian (SL hereinafter) proposed by, for example, Majda and Wang (2001) [13]; and the model introduced by Hwung *et al.* (2011) [14] (H11 hereinafter) based on the downshifting theory developed by Tulin and Waseda [15]. The modified Kato and Oikawa (1995) model (M-KO95 hereinafter) we propose in this paper will be introduced in Sec. V. We also include in our comparison MNLS simulations with no breaking model (labeled NBM). In this section we list the values of the parameters suggested in the literature, which we adopt when studying the perturbed plane-wave cases. For focused wave groups, we use both these parameter values as well as different values, which we obtain through optimization (see Sec. V).

1. Trulsen and Dysthe (1990) (TD90)

To model breaking, Trulsen and Dysthe [11] (TD90) introduced a damping term that turns on when the envelope is steeper than a defined threshold. It is controlled by three parameters:

$$D = -\frac{\omega_0}{2\tau}B\left[\left(\frac{|B|}{B_0}\right)^r - 1\right]H(S - S_0) \quad \text{with} \quad H(x) = \begin{cases} 0 & x < 0, \\ 1 & x \geqslant 0, \end{cases} \tag{12}$$

where we set the nondimensional relaxation time $\tau = 0.125$ (TD90), the breaking strength r is fixed to $r = 2$, and the breaking threshold $S_0 = 0.35$ with $S = k_0|B|$ following TD90; B_0 (>0) is the critical value of $|B|$ when breaking starts, which we obtain from $B_0 = S_0/k_0$. The dissipation terms grows the more $|B|$ exceeds the critical value B_0.

2. Kato and Oikawa (1995) (KO95)

Kato and Oikawa [12] (KO95) model breaking by modifying the return-current term:

$$D = \beta k_0 \frac{\partial\bar{\phi}}{\partial x}B, \tag{13}$$

where we set $\beta = 0.2$ according to KO95. KO95 showed that a positive value of β leads to energy dissipation and an energy flux from higher to lower wave numbers. The dissipation term proposed by KO95 [i.e., (13)] increases in magnitude with larger gradients of the envelope (squared), which
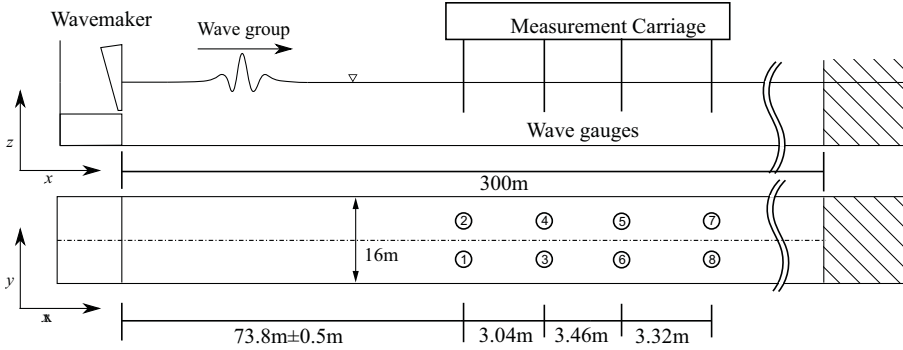
FIG. 1. The gauge layout in the multifunction towing tank at Shanghai Jiao Tong University. The gauges in the 4×2 array are labeled as 1–8. Wave groups travel from left to right.

also drive the return flow [cf. (4)] and will therefore generally be larger after spectral broadening has occurred.

3. Selective Laplacian (SL)

Majda and Wang [13] proposed a dissipation term based on a selective Laplacian (SL). In Fourier space, the selective Laplacian can be written as

$$\hat{D} = \begin{cases} -\beta \frac{\omega_0}{k_0^2}(|k| - k^*)^2 \hat{B}(k) & \text{for} \quad |k| > k^*, \\ 0 & \text{for} \quad |k| \leqslant k^*, \end{cases} \tag{14}$$

where we set $\beta = 0.01$, k is the wave number, k^* is the adjustable threshold value, and we set the $k^* = 1.2k_0$. The selective Laplacian reduces higher-wave-number modes above the threshold value k^*, which leads to energy dissipation and a frequency downshift. Therefore as the spectrum broadens, dissipation will increase.

4. Hwung et al. (2011) (H11)

Hwung *et al.* [14] (H11) introduced a model based on Tulin's downshifting theory [15], which starts from the energy balance of a three-wave system with energy dissipation caused by a plunging breaker, including an explicit parametrization of the shape of the jet formed to determine the energy dissipation. The dissipation term in H11 adds a steepness-based breaking threshold similar to TD90 to the theory to give [15]

$$D = B\left(\frac{D_a}{g|B|^2} + i4\gamma \int \frac{k_0 D_a}{g|B|^2} dx\right) H(S - S_0), \tag{15}$$

where $D_a = \beta\omega_0|B|^4 k_0^2/2$ [14,15], we set $\beta = 0.01$, γ is a breaking strength parameter ranging from 0.4 to 0.7, and we set $\gamma = 0.7$, g is the gravitational constant, the characteristic wave steepness $S_0 = B_0 k_0$ (H11 use $S = \sum a_i k_i$ instead, which is obtained from the discrete Fourier transform of the free surface η), and S_0 is the threshold value of the Heaviside function as in TD90.

C. Laboratory experiments

To assess the ability of the four different reduced-form breaking models to model breaking in focused wave groups, we have performed laboratory experiments in the multifunction towing tank at Shanghai Jiao Tong University, as illustrated schematically in Fig. 1. Waves are generated using a flap-type wave maker. The tank is 300-m long, 16-m wide, and the depth $d = 7.33$ m. The study was

TABLE I. Input parameters for the focused wave groups.

Case	f_0 [Hz]	H_s [m]	σ [Hz]	L_f [m]	$k_0 d$	ϵ	ν
Case 1	0.5	0.35	0.06	144	7.374	0.176	0.12
Case 2	0.5	0.35	0.15	87	7.374	0.176	0.3

restricted to wave breaking in unidirectional waves. Four pairs of resistance-type wave gauges are used, as illustrated in Fig. 1. A sampling frequency of 100 Hz ensures sufficient temporal resolution. As each laterally positioned pair of gauges gives equivalent results, we will henceforth report only four spatial measurements along the length of the flume. The gauges are labeled according to their relative positions to the first gauge: $x = 0$ m (gauges 1 and 2), 3.04 m (gauges 3 and 4), 6.50 m (gauges 5 and 6), and 9.82 m (gauges 7 and 8).

Focused wave groups were generated from a Gaussian surface elevation variance density spectrum:

$$S(f) = \left(\frac{H_s}{4}\right)^2 \frac{1}{\sigma\sqrt{2\pi}}\exp\left[-\frac{(f - f_0)^2}{2\sigma^2}\right], \tag{16}$$

where H_s is the significant wave height, and σ is the spectral bandwidth. We generate waves using the "reverse dispersion method" [25] so that under linear evolution all the phases would focus at a specified point in the wave tank. The parameters of the two cases investigated experimentally are listed in Table I. The focus distance L_f was based on linear theory, as shown in Table I. However, breaking happens before this theoretical distance, namely, at around 77 m from the wave maker for both cases, and the measurement carriage was placed at this location. The steepness ϵ is defined as $\epsilon = k_0 H_s/2$. The bandwidth parameter $\nu = \sqrt{m_2 m_0/m_1^2 - 1}$, where m_n is the nth moment of the variance density spectrum; for the Gaussian spectrum (16), $\nu = \sigma/f_0$. Cases 1 and 2 differ in their spectral bandwidth (and focus distance), with case 2 being more broad banded. Both cases 1 and 2 are repeated 10 times.

In case 1, breaking occurred (repeatedly) between gauge pair 3 and 4 ($x = 3.04$ m) and gauge pair 5 and 6 ($x = 6.50$ m). In case 2, a weak breaking event occurred (repeatedly) between gauge pair 3 and 4 ($x = 3.04$ m) and gauge pair 5 and 6 ($x = 6.50$ m), and a second strong breaking event occurred (repeatedly) between gauge pair 5 and 6 ($x = 6.50$ m) and gauge pair 7 and 8 ($x = 9.82$ m).

D. Initial conditions for the MNLS simulations

In order to compare experiments and MNLS simulations, we "initialize" the simulations using the gauge recordings at the first gauge (gauge pair 1 and 2) instead of starting from the wave-maker position. Accordingly, we set $x = 0$ to correspond to the first gauge (gauge pair 1 and 2).

To convert our surface elevation time series at the first gauge [i.e., $\eta = \eta(x = 0, t)$, a boundary condition] to an initial condition suitable to solve the MNLS equation (3) [i.e., $\hat{B}(k, t = 0)$], we proceed as follows. First, we apply a Fourier transform to the measured surface elevation profile $\eta = \eta(x = 0, t)$ and apply a low-pass filter at $f = 1.86 f_0$ and a high-pass filter at $f = 0.25 f_0$ to remove bound waves. In doing so, we obtain $\hat{B}(x = 0, \omega)$. Second, we use the linear dispersion relation $\omega^2 = gk\tanh(kd)$ to convert the frequency spectrum $\hat{B}(x = 0, \omega)$ to a wave-number spectrum $\hat{B}(k, t = 0)$. We note that water wave dispersion is nonlinear (indeed, this is what the nonlinear terms of the MNLS model) and so this step is an approximation. However, we find that this works acceptably in practice given the agreement between experiment and numerics found in this paper. Third, we set up a linear zone to introduce the wave train. The simulation is configured so that all nonlinear terms including breaking dissipation term are turned off for $x < 0$. The wave field to the left of the first gauge ($x < 0$) evolves linearly, and the wave field to the right of the first gauge ($x > 0$) evolves nonlinearly. This approach is a pragmatic adaptation of the code previous developed in the group,

TABLE II. Input parameters of the perturbed plane-wave cases from [10].

Case	f_0 [Hz]	H_s [m]	$\delta\omega$ [rad/s]	b_F	ψ	k_0d	ϵ
Case 1	1.4	0.051	0.98	0.09	π	6.31	0.20
Case 2	1.5	0.031	1.05	0.06	π	7.24	0.14
Case 3	1.5	0.055	1.05	0.01	π	7.24	0.25
Case 4	1.6	0.039	1.60	0.05	π	8.24	0.20

enabling us to flux waves into the nonlinear part of the simulation. Fourth, we evolve $\hat{B}(k, t = 0)$ in time to $\hat{B}(k, t = t_f)$. Fifth, we perform a fully nonlinear backward MNLS simulation to evolve $\hat{B}(k, t = t_f)$ to $\hat{B}(k, t = 0)$, where the latter is the initial condition we need.

III. PERTURBED PLANE WAVES

In this section we will compare all four models described in Sec. II with parameters used in the literature as reported in Sec. II for the canonical case of perturbed plane waves, where the dynamics are dominated by three modes: a carrier wave and two sidebands. As all four models were developed to explain the key features of wave breaking, namely, a downshift in the mean frequency and energy dissipation, we will focus on these properties. We will compare to recent laboratory experiments of wave breaking for perturbed plane waves in Eeltink *et al.* [10], obtained independently from the theoretical models we compare to.

A. Initial conditions

Theoretically, in the experiment of [10] the wave maker provided the following boundary condition for perturbed plane waves:

$$\eta(0, t) = \frac{H_s}{2}[\sqrt{b_c}\sin(-\omega_0 t) + \sqrt{b_+}\sin(-\omega_+ t + \psi) + \sqrt{b_-}\sin(-\omega_- t + \psi)], \qquad (17)$$

where the upper and lower sideband frequencies are set according to $\omega_\pm = \omega_0 \pm \delta\omega$, with $\delta\omega$ the modulational frequency, and ψ is the phase shift of the sidebands compared to the carrier wave. The sideband wave numbers $k_\pm$ are calculated using the linear dispersion relationship $\omega_\pm^2 = gk_\pm \tanh(k_\pm d)$. The amplitudes of the carrier wave and the upper and lower sidebands are set according to $a_c = H_s\sqrt{b_c}/2$, $a_+ = H_s\sqrt{b_+}/2$, and $a_- = H_s\sqrt{b_-}/2$, where $b_c = 1 - b_F$, $b_+ = (1 - b_c)/2$, and $b_- = (1 - b_c)/2$, respectively, and b_F is sideband fraction. The water depth $d = 0.8$ m. The parameters of the four breaking cases from [10] we consider are listed in Table II. In these experiments, the wave maker is located at $x = 0$ m and the gauges are labeled based on their relative positions to the wave maker. We compare MNLS simulation with time series data recorded from six gauges: $x = 3.79$ m, 8.82 m, 13.73 m, 18.78 m, 24.53 m, and 29.10 m.

In practice, instead of using Eq. (17), the initial wave field for MNLS simulation is recovered from the measurement of the first gauge following steps 1 and 2 described in Sec. II D so that the surface elevation profile of the first gauge is reproduced exactly. Then we perform the MNLS simulation with the linear zone and boundary conditions specified above.

B. Comparison of breaking models

Figure 2 shows the surface elevation for case 1 in Table II at the different gauge locations, where we have moved into the reference frame of the group by shifting in time by $x/c_{g,0}$, with x the gauge location and $c_{g,0} = \omega_0/(2k_0)$ the group speed, comparing experimental data of [10] to (a) MNLS
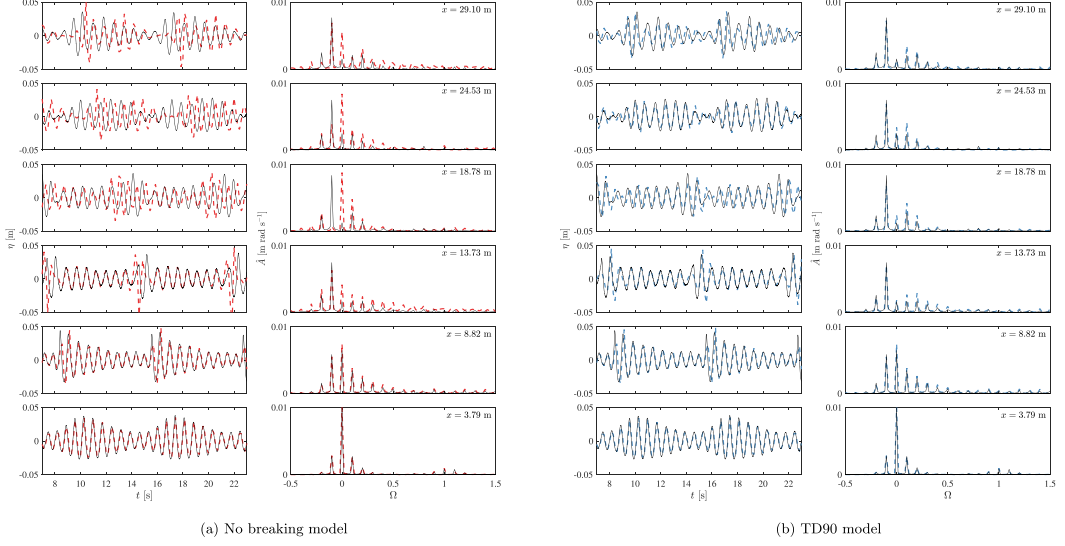
(a) No breaking model

(b) TD90 model

FIG. 2. Surface elevations and amplitude spectra at different gauge locations for perturbed plane waves (case 1 in Table II). Black solid lines correspond to experimental data, and colored dashed lines to MNLS simulations (a) without a breaking model and (b) with the breaking model of TD90. For the wave spectra, we use $\Omega = \omega/\omega_0 - 1$.

solutions without a breaking model and (b) MNLS solutions with the breaking model of TD90. The figure illustrates that the wave train experiences a partial modulation-demodulation cycle as expected for a perturbed plane wave. The MNLS simulation without a breaking model produces an excessively tall focused wave, as is evident from the surface elevation profile, and fails to predict a downshift in the frequency spectrum. Instead, the MNLS simulation with the breaking model of TD90 predicts a frequency downshift with a slight overestimation of the effect on the upper sideband, and the predicted surface elevation profile and frequency spectrum closely match the experimental results.

To examine all four reduced-form breaking models, Fig. 3 compares MNLS simulations for each model to experimental data for case 1 in Table II. Figure 3 examines the evolution of the three modes of the perturbed plane wave, spectral properties, and energy conservation. Panels (a)–(c) respectively show the evolution of the carrier wave, the lower sideband, and the upper sideband. The TD90 (and the modified M-KO95 model), which will be introduced in Sec. V, gives the best prediction for the spatial evolution of the carrier wave amplitude. The TD90, SL, and M-KO95 models give a reasonably good prediction for the lower sideband. The SL model gives the best prediction for the upper sideband.

In panel (d) it is seen that the TD90, SL, and M-KO95 models give a good match for the evolution of the spectral peak $\Omega_{\text{peak}} = \text{argmax}_\Omega \hat{A}$ with $\Omega = \omega/\omega_0 - 1$ and $\hat{A}(\Omega)$ the amplitude spectrum, where we note only three values of Ω_{peak} are possible: -0.1, 0, and 0.1, corresponding to the lower sideband, the carrier wave, and the upper sideband, respectively.

In panel (e), the SL model matches best to experiments in terms of the evolution of the spectral mean, $\Omega_{\text{center}} = \sum \Omega_i \hat{A}_i / \sum \hat{A}_i$, while all other models have an upward bias compared to experiments. For energy conservation, panel (f), although the experimental data shows considerable variability, it seems that the TD90 model (and the M-KO95 model) gives the most reasonable prediction of the energy evolution in experiments, with the other models underestimating the amount of energy lost due to breaking. The reader is referred to Appendix A for similar figures for the other three cases in Table II, which lead to qualitatively similar conclusions.
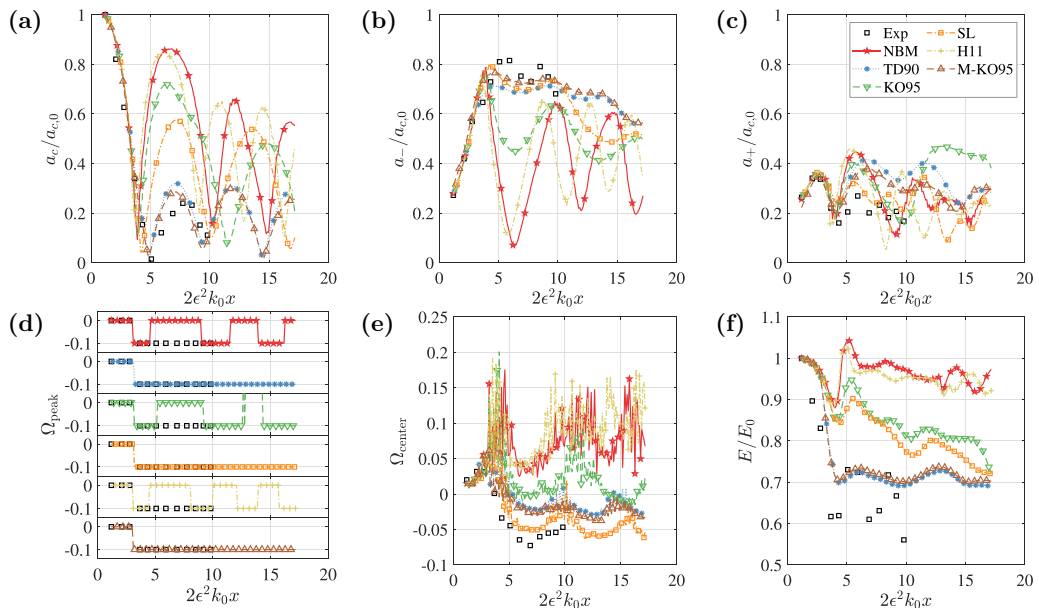
FIG. 3. Spatial evolution of perturbed plane waves for different reduced-from breaking models including no breaking model (NBM), showing (a) the carrier wave normalized by its value at the first gauge, $a_c/a_{c,0}$; (b) the normalized lower sideband $a_-/a_{c,0}$; (c) the normalized upper sideband, $a_+/a_{c,0}$; (d) the spectral peak, $\Omega_{\text{peak}} = \text{argmax}_\Omega \hat{A}$ with $\hat{A}$ the amplitude spectrum of η and $\Omega = \omega/\omega_0 - 1$; (e) spectral mean or centroid, $\Omega_{\text{center}} = \int \Omega(\omega)\hat{A}(\omega)d\omega / \int \hat{A}(\omega)d\omega$; and (f) the energy measure $E = \int |B|^2\, dt$ normalized by its value at the first gauge E_0. The black squares show the experimental data from [10] (case 1 from Table II).

IV. FOCUSED WAVE GROUPS

In this section we will compare the experiments obtained herein for dispersively focused wave groups (see Sec. II C) with MNLS simulations using the breaking models with parameter values taken from the literature as given in Sec. II B. We will examine optimized parameter values in Sec. V.

A. Effects of breaking

Figure 4 shows the surface elevation for case 1 in Table I at the different gauge locations, comparing experimental data to (a) MNLS solutions without a breaking model and (b) MNLS solutions with the breaking model of TD90. Breaking occurs between $x = 3.04$ m and $x = 6.50$ m. At $x = 6.50$ m, the first (leftmost) large crest is neither described well by the MNLS simulations without breaking model nor by those with the breaking model of TD90. Both underestimate the surface elevation of the crest compared to experiments. We note that this crest did not actually break in experiments; the difference between simulations and experiments very probably arises because of the inherent limitation of the MNLS equation to model only relatively narrow-banded highly nonlinear waves, as demonstrated in previous work [23]. It is only the second (from the left) crest (between $t = 102$ s and $t = 105$ s) at $x = 6.50$ m in Fig. 4 that actually breaks, as can be confirmed from video recordings. Here, the MNLS without breaking model predicts an excessively high crest [panel (a)], which is not observed in experiments. The TD90 model predicts the reduction of the excessively high crest reasonably well in the time domain.

In the amplitude spectra in Fig. 6, breaking manifests itself as an effect on the right-hand-side "shoulder" of the spectrum (i.e., at approximately $\Omega = 0.22$). Such phenomena has been observed
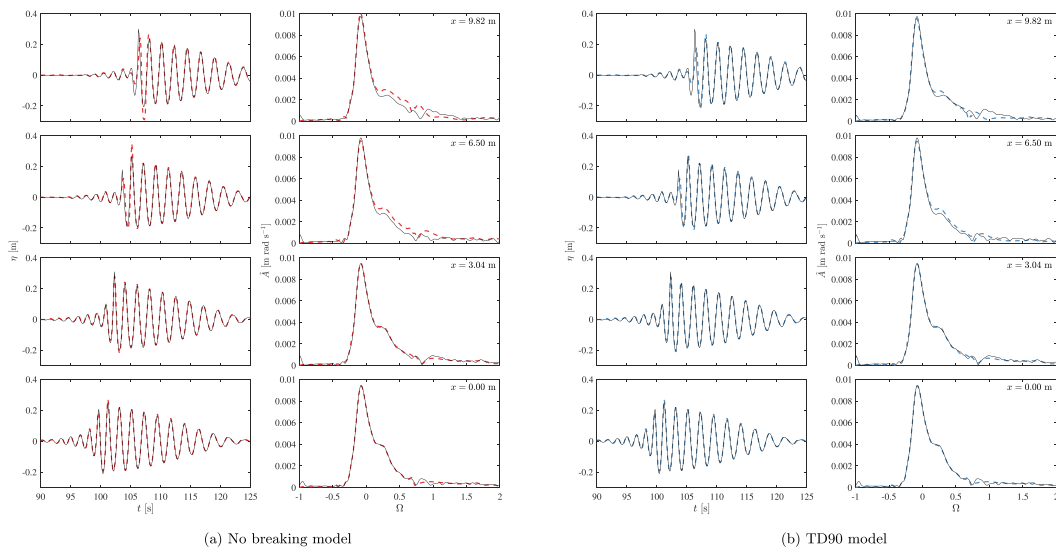
(a) No breaking model

(b) TD90 model

FIG. 4. Surface elevations and amplitude spectra at different gauge locations for focused wave groups (case 1 in Table I). Black solid lines correspond to experimental data and colored dashed lines to MNLS simulations (a) without a breaking model and (b) with the breaking model of TD90. For the wave spectra, we use $\Omega = \omega/\omega_0 - 1$.

and discussed in the past literature [26,27]. Comparing the magnitude of the spectra between $x = 3.04$ m (before breaking) and $x = 6.50$ m (after breaking), a clear reduction of the spectral shoulder is evident, which is neither correctly predicted by the MNLS simulations without a breaking model nor by those with the breaking model of TD90.

B. Comparison of breaking models

1. Comparison based on the time domain

Figure 5 shows the surface elevation predicted by the four reduced-form breaking models. The major difference between the models is whether the second steepest crest at $x = 6.50$ m is suppressed. In MNLS simulations without a breaking model, the second steepest crest after breaking is overestimated by 10% compared to experiments. Unlike TD90 in Fig. 4, all three other models, KO95, SL, and H11, do not lead to significantly improved agreement with the experimental data compared to the case with no breaking model (cf. Fig. 4).

2. Comparison based on the frequency domain

By examining the amplitude spectrum before and after breaking, Fig. 6 examines the ability of the different reduced-form breaking models to capture the effect of breaking on the spectrum of a wave group (for both cases 1 and 2). By showing confidence bands (gray shaded regions) corresponding to one standard deviation on either side of the mean obtained from 10 repeated experiments, the figure first shows that dissipation of the right-hand-side spectral shoulder is a robust feature of breaking. Although most models (except for SL) reproduce this shoulder before breaking ($x = 3.42$ m) and most models predict some kind of reduction in its magnitude after breaking ($x = 6.50$ m) (except for SL), all of the models underestimate the amount of energy dissipated in the shoulder by breaking.
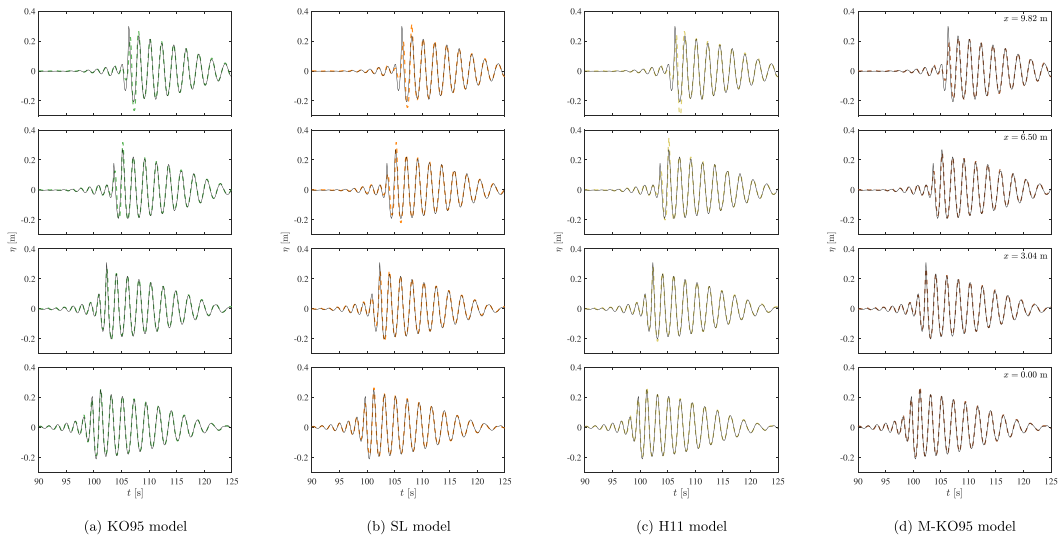
FIG. 5. Surface elevations at different gauge locations for focused wave groups (case 1 in Table I). Black solid lines correspond to experimental data and colored dashed lines to MNLS simulations (a) with the model of KO95; (b) with the SL model; (c) with the model of H11; and (d) with the M-KO95 model.

3. Comparison based on phase

Having examined the effect of breaking on the magnitude of the spectrum, Fig. 7 examines whether breaking affects phase. In Fig. 7 we show the phase difference between two consecutive gauges, where we have accounted for linear phase change $k\Delta x$ with Δx the distance between gauges. Although nonlinearity causes a consistent phase shift, we are not able to find any obvious phase distortion caused by wave breaking. The large-amplitude oscillations in Fig. 7 for small Ω in the narrow-banded case arise because the very small amplitudes of the spectrum for small Ω, will be affected by bound waves and are therefore ignored here.

V. BREAKING MODEL OPTIMIZATION AND MODIFICATION

In Sec. IV we have used parameter values for the four reduced-form breaking models suggested in the literature for perturbed plane waves (given in Sec. II B) to model breaking in focused wave groups. To examine whether the performance of these models for focused wave groups can be improved, we will select parameters that minimize the least-squares difference between predictions and experiments we have carried out. In doing so, we will also examine the performance and additional benefit of incorporating three different breaking criteria, which we apply to each of the four reduced-form breaking models (noting that TD90 and H11 already include breaking criteria). Finally, we will examine what type of (heuristic) modification of the breaking models can further improve agreement with experimental data.

A. Breaking criteria

Three breaking criteria are implemented: a local geometric criterion, a local kinematic criterion, and a global kinematic criterion with a fixed-duration active breaking interval:

(1) The local geometric breaking criterion, $H(S > S_0)$, is based on wave steepness S and is equivalent to the criterion already included in the breaking models of TD90 and H11. Steepness $S = k_0|B|$ is defined by the magnitude of the envelope multiplied by the carrier wave number. For perturbed plane waves we have set $S_0 = 0.35$, but for focused wave groups we had to adjust S_0 to

(a) Case 1, Before breaking ($x = 3.04$ m).

(b) Case 1, After breaking ($x = 6.50$ m).

(c) Case 2, Before breaking ($x = 3.04$ m).

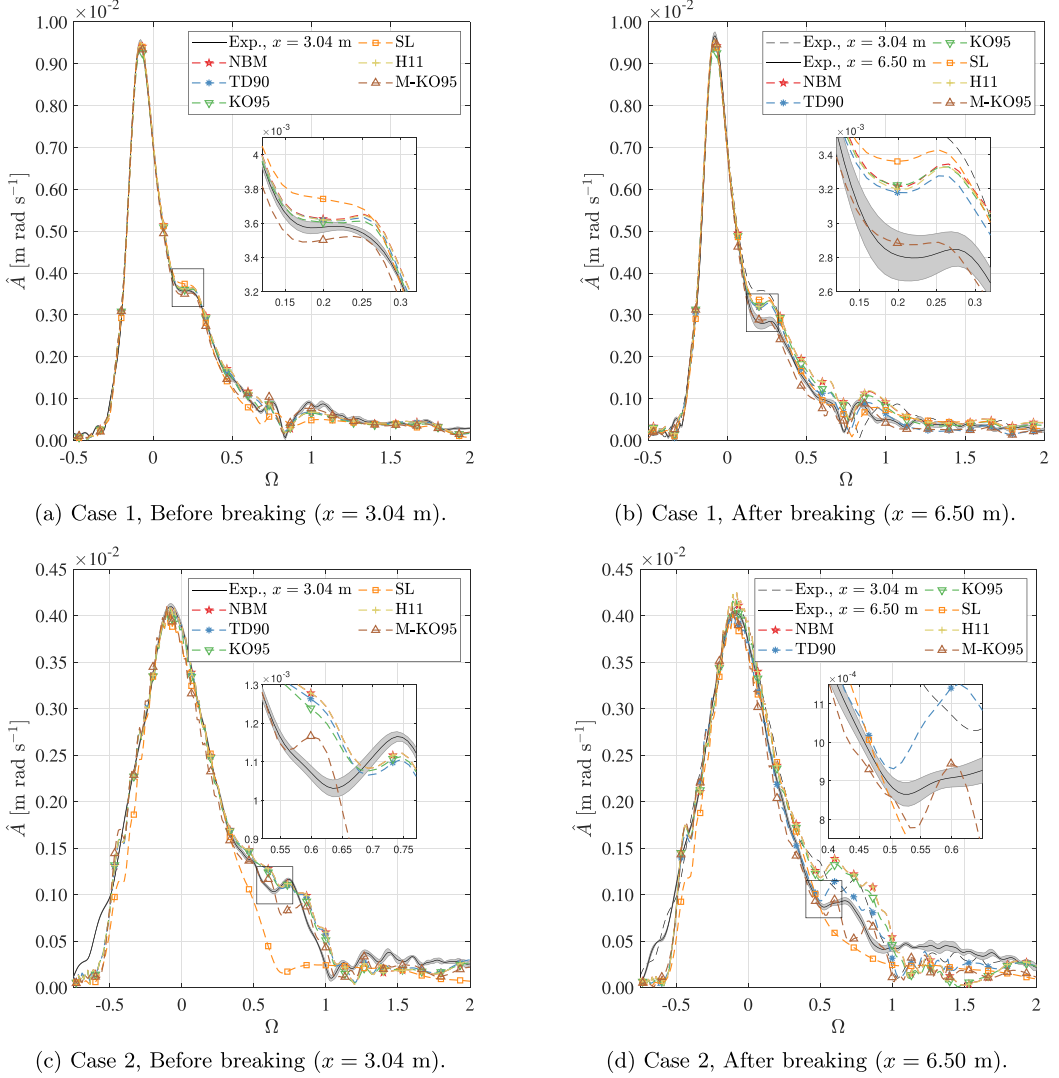(d) Case 2, After breaking ($x = 6.50$ m).

FIG. 6. Comparison of amplitude spectra before and after breaking of a focused wave group (see Table I) for different reduced-form breaking models including no breaking model (NBM), showing experiments (black solid/dashed lines), with gray shaded region corresponding to ± 1 standard deviation from repeated experiments, and MNLS simulations with different breaking models (colored dashed lines with markers).

match the onset of breaking in video recordings of the experiments. We do this by inspecting video recordings of the wave-tank experiments and recording the time at which white-capping starts to develop. We then choose S_0 in MNLS simulations so that the breaking onset occurs at the same time. We thus set $S_0 = 0.24$ and $S_0 = 0.19$ for cases 1 and 2, respectively.

(2) The local kinematic breaking criterion, $H(u/c > 0.88)$ from [28], is based on the ratio of the horizontal fluid speed u and the crest speed c. The former is obtained from the potential (cf. $u = \partial \phi / \partial x$), which is reconstructed up to $O(\epsilon^3)$ according to [29]

$$\phi(x, z, t) = \left[\frac{i\epsilon\omega_0}{k_0}\tilde{B} + \frac{\epsilon^2\omega_0}{2k_0^2}\tilde{B}_x + \epsilon^3\left(-\frac{ik_0\omega_0}{2}|\tilde{B}|^2\tilde{B}_x - \frac{3i\omega_0}{8k_0^3}\tilde{B}_{xx} \right) \right] e^{i(k_0 x - \omega_0 t) + k_0 z} + \text{c.c.}, \quad (18)$$

(a) Case 1 (narrow-banded).
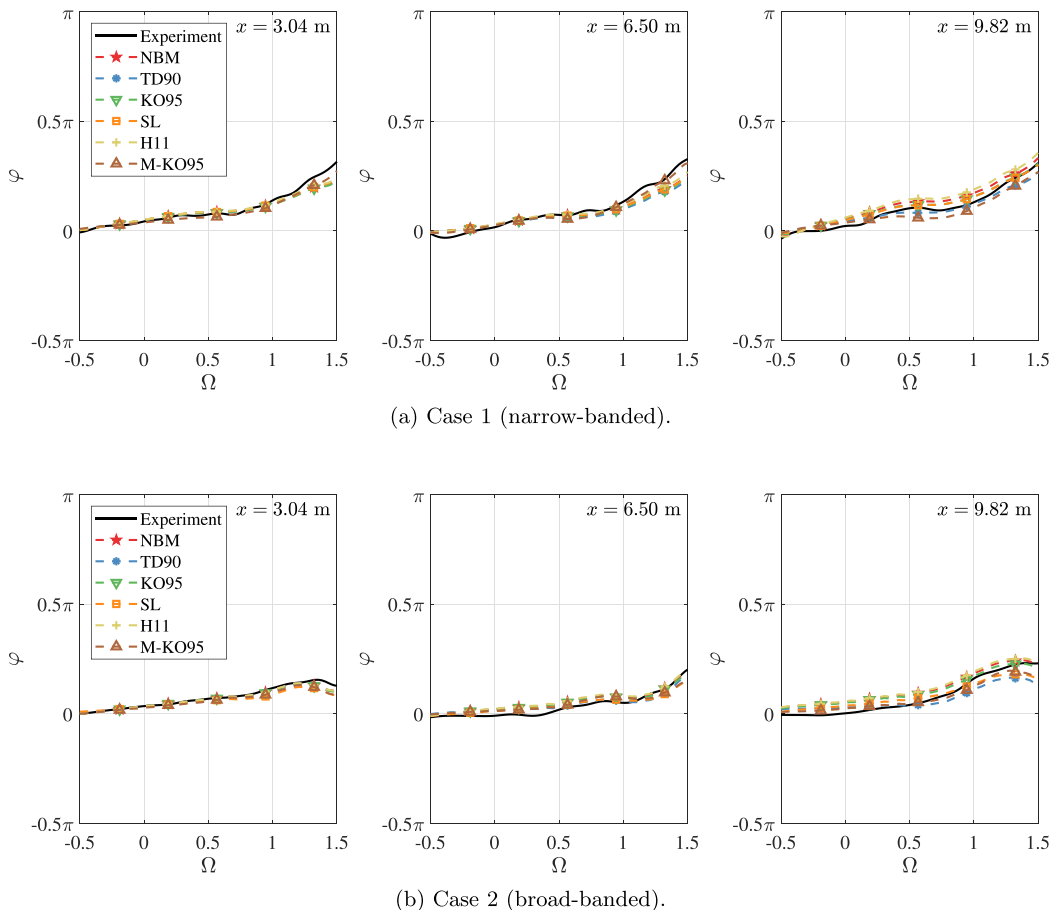

(b) Case 2 (broad-banded).

FIG. 7. Phase difference between consecutive gauges for case 1 (a) and case 2 (b) for focused wave groups in Table I (with the labels corresponding to the gauge with the largest x), comparing experiments (black lines), MNLS simulations with no breaking model (NBM, red dashed lines), and with the breaking models (colored dashed lines). In case 1, breaking occurred between gauge $x = 3.04$ m and $x = 6.50$ m. In case 2, a weak breaking event occurred between $x = 3.04$ m and $x = 6.50$ m, and a second strong breaking event occurred between $x = 6.50$ m and $x = 9.82$ m.

where $\tilde{B} = Be^{k_0 z}$, we set $z = \eta_1$, and c.c. represents the complex conjugate. We ignore the effect of bound waves on the velocity. The breaking crest speed c is approximated by $0.8\omega_0/k_0$. The breaking criterion is local, meaning it is applied only at those locations where $u/c > 0.88$.

(3) The global kinematic breaking criterion, $H(u/c > 0.88)$, will turn on globally for a fixed time interval T_b whenever the kinematic breaking criterion is triggered at any location as detailed in [30]. The active breaking time interval $T_b = 0.75 \times [2\pi/(k_b c_b)]$ [30], where we set $c_b = 0.8\omega_0/k_0$ and we assume $k_b = k_{\text{local}}$ with the latter obtained from [31]:

$$k_{\text{local}}(x, t) = \frac{1}{\eta^2 + \mathcal{H}^2(\eta)} \left(\eta \frac{\partial}{\partial x} \mathcal{H}(\eta) - \mathcal{H}(\eta) \frac{\partial}{\partial x} \eta \right), \qquad (19)$$

where $\mathcal{H}$ is a Hilbert transform. By choosing k_b when the kinematic breaking criterion $H(u/c > 0.88)$ is satisfied at multiple locations, we take the maximum value and apply it globally. Such treatment works for all the cases in this study, as only one breaking event is ever active at the same time.

TABLE III. Results from parameter optimization and modification of the reduced-form breaking models (NBM denotes the case with no breaking model). The L2 loss is normalized by its value for the case with no breaking model.

Model	Optimized (Y/N)	Breaking criterion	L2 loss (case 1)	L2 loss (case 2)	Parameter (τ, β)
NBM	N	None	1.00	1.00	–
TD90	N	Geometric	0.85	0.90	0.125
TD90	Y	Geometric	0.83	0.92	1.425
TD90	Y	Kinetic	0.85	0.94	0.138
TD90	Y	Fixed interval	0.83	0.92	1.375
KO95	N	None	0.99	0.94	0.2
KO95	Y	None	0.98	0.96	0.116
KO95	Y	Geometric	0.84	0.92	1.485
KO95	Y	Kinetic	0.89	0.94	6.504
KO95	Y	Fixed interval	0.82	0.88	1.384
SL	N	None	1.01	0.95	0.01
SL	Y	None	0.97	0.98	0.003
SL	Y	Geometric	0.93	0.97	0.0148
SL	Y	Kinetic	0.92	0.97	0.0663
SL	Y	Fixed interval	0.67	0.94	0.0475
H11	N	Geometric	0.97	1.00	0.01
H11	Y	Geometric	0.97	1.00	0.0676
H11	Y	Kinetic	0.65	0.99	1.323
H11	Y	Fixed interval	1.00	1.00	0.001
M-KO95	Y	Geometric	0.68	0.90	Fig. 8
M-KO95	Y	Kinetic	0.52	0.92	Fig. 8
M-KO95	Y	**Fixed interval**	**0.52**	**0.80**	**Fig. 8**

B. Parameter optimization

By comparing the surface elevation profile before ($x = 3.04$ m) and after ($x = 6.50$ m) breaking in Fig. 4, it is evident that the MNLS simulations agree well with the experimental data before but not after breaking. Thus, in order to improve performance of the different models, we use the experimental data to obtain a value of the prefactor β in the dissipation terms (or τ in the case of TD90) that lead to better agreement. In particular, we choose a prefactor β, which we henceforth term the dissipation strength parameter, that minimizes the squared difference between the MNLS prediction (with breaking model and breaking criterion) and the measured surface elevation at the gauge(s) after breaking, which we term the L2 loss:

$$\beta^* = \underset{\beta}{\mathrm{argmin}} \sum_t (\eta_{\mathrm{MNLS}}[t, x = (6.50\,\mathrm{m}, 9.82\,\mathrm{m}); \beta] - \eta_{\mathrm{experiment}}[t, x = (6.50\,\mathrm{m}, 9.82\,\mathrm{m})])^2, \quad (20)$$

where the sum is taken over the discrete sampling times t, and we use fixed experimental durations of 60 s. We use case 1 to obtain β^*, combining gauges at $x = 6.50$ m and $x = 9.82$ m.

Table III shows the L2 loss for case 1 after optimization according to (20) for the four different reduced-form breaking models with different breaking criteria (described in Sec. V A), as well as the corresponding dissipation strength parameter β^* (or τ^* in the case of TD90). Also shown is the L2 loss for case 2, which is evaluated using the dissipation strength parameter β^* obtained by optimization for case 1. It is evident that existing models achieve significantly better performance with optimized parameters for case 1. In general, the L2 loss in the time domain for both focused

wave cases with optimized parameters decreases compared to the same two cases with values from the literature (for perturbed plane waves). While the optimization is performed for case 1, the L2 loss for case 2 is also improved, albeit to a lesser extent. We do not observe consistent differences in performance of the different breaking criteria between the different reduced-form models, although inclusion of a breaking criterion generally reduces the L2 error.

Figure 14 in Appendix B shows the time-domain comparison with experiments for the four reduced-form breaking models with optimized parameters, where we show only the breaking criterion that corresponds to the lowest L2 error in Table III for each. Compared to the case with values of the parameters from the literature, only modest improvements in the agreement of the surface elevation of the breaking crests with experiments is obtained with the optimized parameters. In the frequency domain, none of the four models with optimized parameters can correctly predict the dissipation of the shoulder of the spectrum that we have observed in Fig. 6 (see Fig. 15 in Appendix B, where we show only the breaking criterion that corresponds to the lowest L2 error in Table III for each).

C. Model modification

To examine whether still better agreement with experimental data can be obtained, we take the following heuristic approach. We replace the dissipation strength parameter β in D by a spectral dissipation strength parameter $\hat{\beta}(k)$, which is a function of wave number k and allows a different weight to be placed on different wave numbers contributing to the dissipation term. For the Kato and Oikawa [12] (KO95) model (henceforth the modified Kato and Oikawa model, M-KO95), this modification takes the form

$$D = k_0 B \mathcal{F}^{-1} \left\{ \hat{\beta}(k) \mathcal{F} \left\{ \frac{\partial \bar{\phi}}{\partial x} \right\} \right\} H, \tag{21}$$

where $\mathcal{F}$ denotes a Fourier transform, and H is the Heaviside function corresponding to one of the three breaking criteria. We require all the components of $\hat{\beta}(k)$ to be real. Equations for the three other modified models are given in Appendix B.

We use MATLAB's trust region reflective algorithm to obtain $\hat{\beta}(k)$ according to (20). Specifically, we use 20 control points to define $\hat{\beta}(k)$ between $k = 0$ and $k = 3k_0$ and then interpolate linearly to reconstruct the curve in order to reduce computational cost. The result is not sensitive to spatial and temporal resolution of the MNLS solver or the number of control points. We only present the results for the modified Kato and Oikawa model (M-KO95) with a fixed-interval breaking criterion and note that only modified models with a fixed-interval breaking criterion can predict the dissipation near the "shoulder" in the spectrum correctly. We choose the M-KO95 model as it achieves the lowest L2 loss for case 2. The optimal spectral dissipation strength parameter $\hat{\beta}(k)$ for the M-KO95 model is shown in Fig. 8 for the three different breaking criteria. From this figure, it is clear that dissipation should generally be even stronger for higher wave numbers, noting that the effect of wave numbers greater than $2k_0$ ($\lambda = 1$) will be weak, as there is little energy at such high frequencies.

D. Performance of the modified Kato and Oikawa (M-KO95) model

In this section we will examine performance of the modified M-KO95 model with the fixed-interval breaking criterion for perturbed plane waves and focused wave groups.

1. Perturbed plane waves

Although we have obtained values of the spectral dissipation strength by fitting to experiments for focused wave groups, the M-KO95 model also performs remarkably well for the perturbed plane waves we have considered in Sec. III. In Fig. 3 we find that the M-KO95 model gives the closest prediction of the amplitude of the carrier wave. For the lower and upper sidebands, the performance of the M-KO95 model is as good as existing models. For all other metrics in Fig. 3
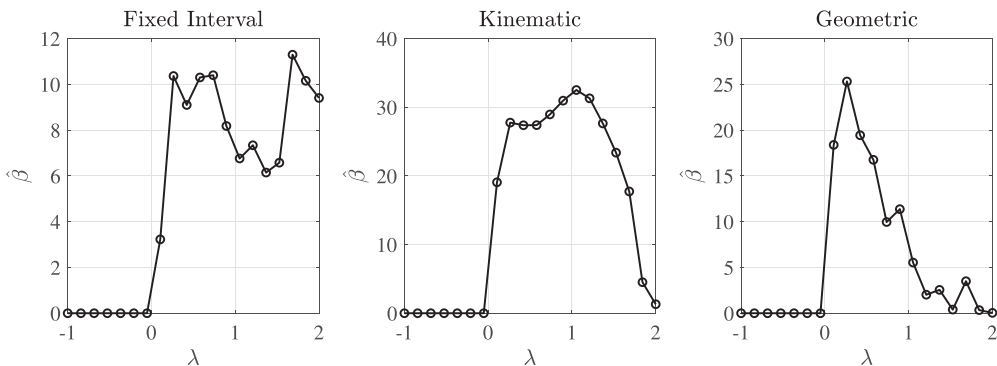
FIG. 8. Optimal spectral dissipation strength parameter $\hat{\beta}$ as a function of $\lambda = k/k_0 - 1$ for the modified Kato and Oikawa [12] model (M-KO95) for three different breaking criteria. The open circles are the actual control points, and any values in between two points are reconstructed by linear interpolation.

the M-KO95 model also gives reasonable predictions, suggesting a certain robustness and generality of the modified model.

2. Focused wave groups

Starting with the time domain, it is clear from Fig. 5 that the M-KO95 model captures the reduction of the amplitude of the breaking crests in the experiments very well. In Fig. 6 we can compare the performance of the M-KO95 model to the original (nonmodified and with parameter values from the literature) reduced-form breaking models. Only the M-KO95 model predicts the correct dissipation of the shoulder of the frequency spectrum.

Figure 9 examines how the M-KO95 models breaking by showing the spatial distribution of the dissipation term and its effect on the envelope at the start and end of the breaking event. Also shown is the reconstructed surface elevation as an indicator of the phase of the surface elevation. From the top panels it is clear that dissipation is strongest at the front of the wave groups, where the envelope is suppressed by the breaking term (see bottom panels). In Fig. 10 we further examine the behavior of the M-KO95 model. It is evident that breaking is only activated for three discrete events as a result of the implementation of the breaking criterion. It is evident that a downshift of the spectral mean takes place when MNLS simulations with no breaking model would predict an increase due to nonlinear wave interactions. A total of 10%–15% of energy is dissipated during breaking. The energy flux reflects the symmetry of the wave spectrum, and a positive flux indicates that the energy flows from high to low frequencies (cf. [12]).

VI. CONCLUSIONS

In this paper we have reviewed the performance of existing reduced-form breaking models that can be added as a dissipation term to the modified nonlinear Schrödinger (MNLS) equation, which together describe the envelope evolution of breaking deep-water waves. In particular, we have examined the breaking models by Trulsen and Dysthe (1990) [11], Kato and Oikawa (1995) [12], Hwung *et al.* (2011) [14], and the selective Laplacian (used, for example, in [13]). We have reviewed their performance for two wave types: perturbed plane waves and focused wave groups.

Perturbed plane waves initially consist of three distinct modes: the carrier wave and two sidebands. During propagation, nonlinear modulation causes the spectrum to broaden. The point of maximum steepness corresponds to the point of maximum spectral width. Wave breaking induces a permanent downshift by dissipating the energy of the upper sideband and thereby the total energy and causing the lower sideband to grow. We have found that for perturbed plane waves, the four models can qualitatively and quantitatively predict these effects of breaking.
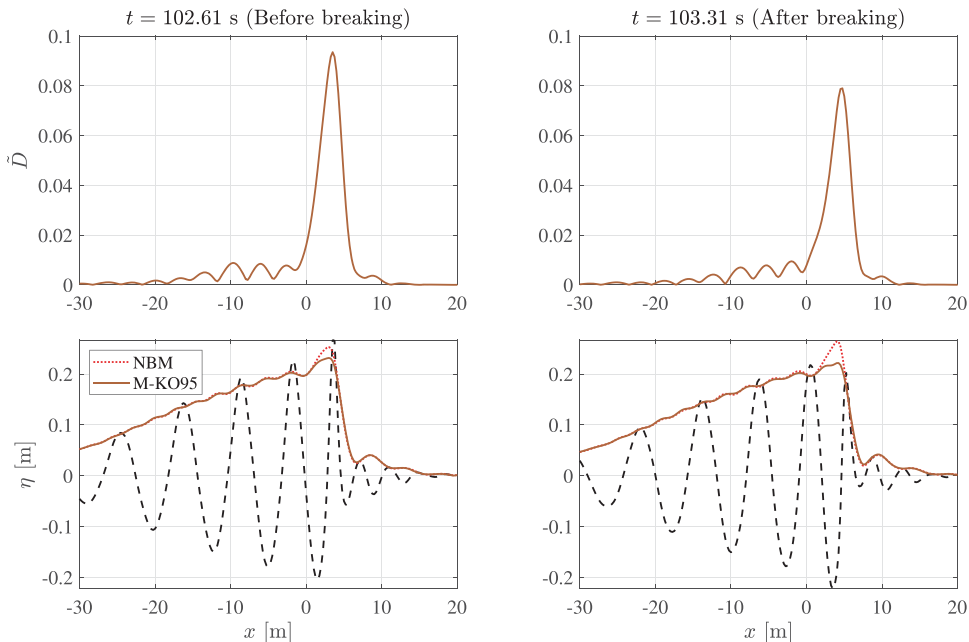
FIG. 9. Spatial distribution of the normalized dissipation term $\tilde{D} = 2\epsilon k_0/\omega_0 D$ (top panels) aligned with the envelope for simulations with no breaking model (NBM) and with the M-KO95 model (bottom panels), for which the dissipation term is examined in the top panels, at the start (or just before, left), and at the end (or just after, right) breaking for a focused wave group (case 1 in Table I). The dashed black line corresponds to the surface elevation from MNLS simulations with no breaking model, the red dotted line is the envelope from MNLS simulations with no breaking model (NBM), and the brown solid line in the bottom panels is envelope from MNLS simulations with the M-KO95 model.

For focused wave groups, the maximum steepness is obtained primarily through alignment of the phases. We observe that wave breaking modifies 1 to 2 crests at the front of the wave group. The high-frequency part of the spectrum is selectively dissipated during breaking, taking the form of a distinct high-frequency shoulder that looses energy due to breaking in our experiments. For these waves with a continuous spectrum, all models fail to produce the correct spectral dissipation, both with values of the parameters suggested in the literature for perturbed plane waves and values obtained by optimization in the time domain based on wave group experiments are used.

As all the reduced-form breaking models "activate" when the spectrum broadens (or the wave group narrows), this explains their effectiveness for perturbed plane waves. For focused wave groups, spectral broadening is not equally effective at "detecting" wave breaking, although the use of breaking criteria can help. Combining the ideas of the different breaking models, we introduce a heuristic approach to modify existing models to predict breaking in wave groups.

Specifically, we propose to add a breaking criterion (a global kinematic criterion that turns on for a finite time interval works best) to the model of Kato and Oikawa (1995) [12] and make the dissipation strength parameter wave number dependent, resulting in what we term the modified Kato and Oikawa model (M-KO95). Optimized on focused wave groups and with a large number of free parameters included in the spectral dissipation strength parameter, unsurprisingly, this model is able to correctly approximate the spectral dissipation observed in our experiments. More insightful is that it generalizes well to perturbed plane waves. Indeed, the M-KO95 model outperforms existing breaking models for both the perturbed plane waves and focused wave groups. The selective dissipation of even higher wave numbers compared to the nonmodified models that is required

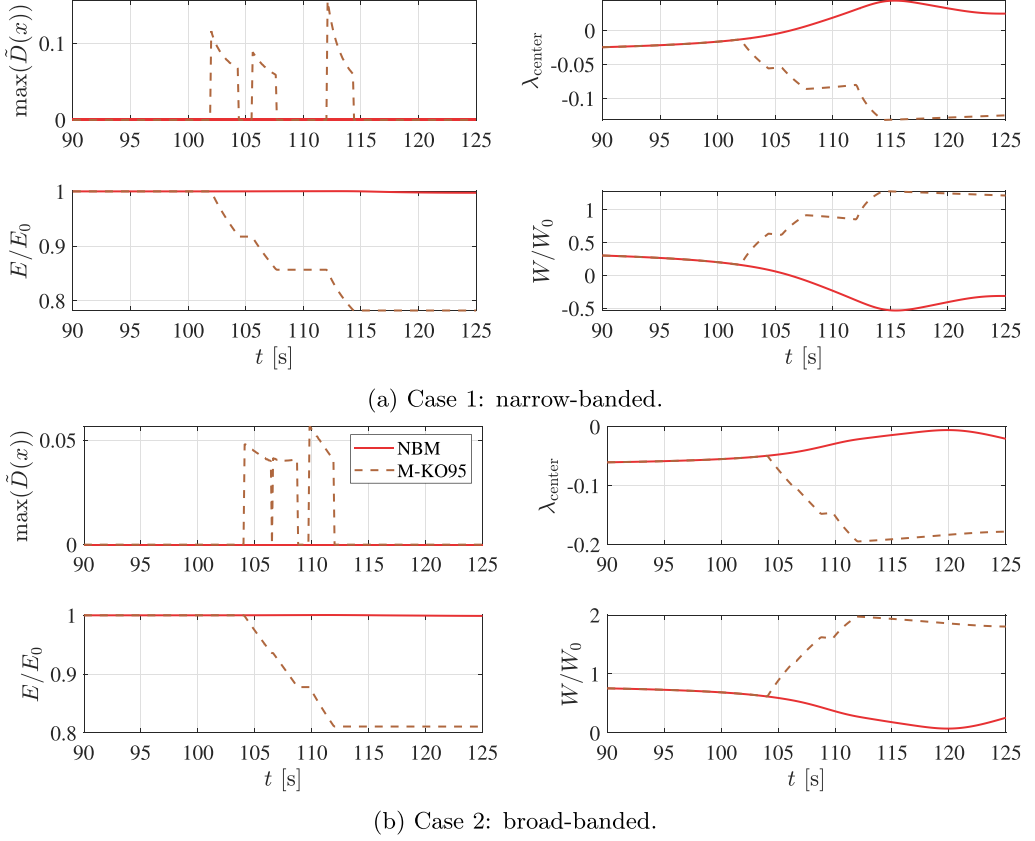(a) Case 1: narrow-banded.

(b) Case 2: broad-banded.

FIG. 10. Temporal evolution before, during, and after breaking according to MNLS simulations with the M-KO95 model for focused wave groups (Table I), showing activation of the dissipation term (top left), the normalized spectral mean $\lambda_{\text{center}} = \int \lambda(k)\hat{A}(k)\,dk / \int \hat{A}(k)\,dk$ (top right), the energy measure $E = \int |B|^2\,dx$ normalized by its initial value (bottom left), and the energy flux defined as $W = \int B^*(\partial B/\partial x) - B(\partial B^*/\partial x)\,dx$, which is normalized by $W_0 = E_0 k_0 / 2\pi$ (bottom right).

for this result should inform the development of new reduced-form wave breaking models for wave groups and random seas in the future.

APPENDIX A: COMPARISON FOR ADDITIONAL PERTURBED PLANE-WAVE CASES

Figures 11–13 show the comparison with experimental data for the additional three cases from [10] in Table II. Figure 11 shows the nonbreaking experiment (case 2). The breaking models that include a breaking criterion (TD90 and H11) are not turned on or are only turned on briefly with only a weak breaking effect, and resulting predictions are equivalent (or very similar) to the case
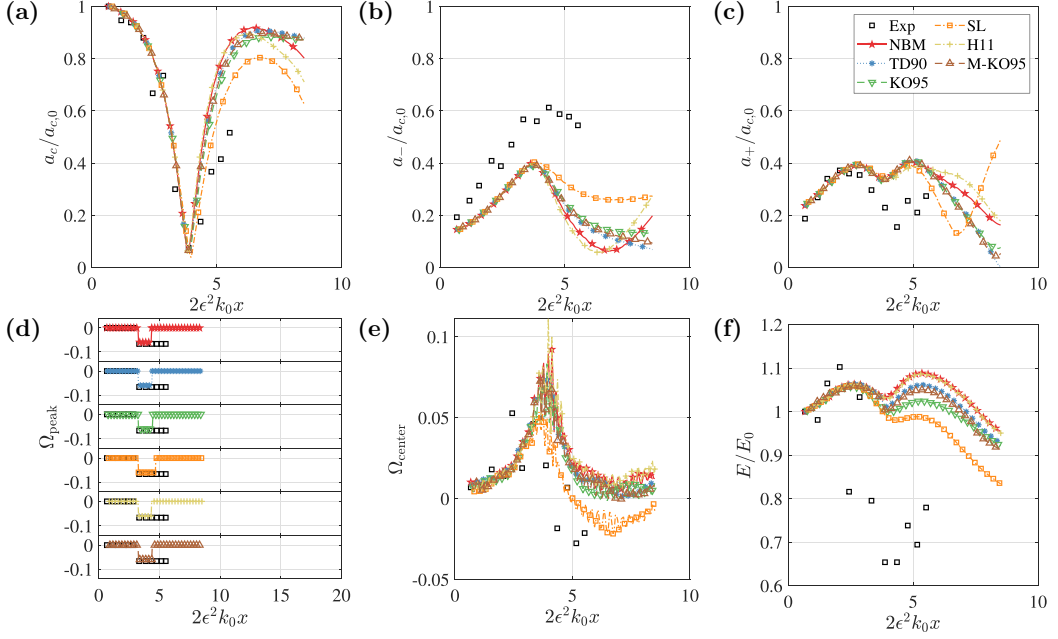
FIG. 11. Similar to Fig. 3 but for case 2 from Table II: spatial evolution of perturbed plane waves, showing (a) the carrier wave normalized by its value at the first gauge, $a_c/a_{c,0}$; (b) the normalized lower sideband $a_-/a_{c,0}$; (c) the normalized upper sideband, $a_+/a_{c,0}$; (d) the spectral peak, $\Omega_{peak} = \mathrm{argmax}_\Omega \hat{A}$, with $\hat{A}$ the amplitude spectrum of η and $\Omega = \omega/\omega_0 - 1$; (e) spectral mean or centroid, $\Omega_{center} = \sum \Omega_i \hat{A}_i / \sum \hat{A}_i$; (f) the energy measure $E = \int |B|^2 \, dt$ normalized by its value at the first gauge E_0. The black squares show the experimental data from [10]).

with no breaking model (NBM). No significant permanent downshift is observed, but we emphasize that considerable difference between experiments and MNLS predictions remains. Figure 12 shows case 3, which has the largest steepness among the four cases. We find that the M-KO95 model achieves the best match of the amplitude of the carrier wave, while all the models underestimate the amplitude of the lower sideband. In Fig. 13, the M-KO95 and KO95 models match best to experimental data in terms of the carrier wave amplitude. All models can match the amplitudes of upper and lower sidebands reasonably well.

APPENDIX B: PERFORMANCE OF OTHER MODIFIED MODELS

In Sec. V C we introduced a method to modify existing reduced-form breaking models by adding a spectrally weighted dissipation strength parameter as well different breaking criteria. In Sec. V D we presented results for the M-KO95 model. In this section we will examine modification of the other three models and evaluate their performance compared to our focused wave experiments.

Modified Trulsen and Dysthe (1990) model (M-TD90)

The modified Trulsen and Dysthe (1990) (M-TD90) model has the form

$$D = -\frac{1}{\tau} B \mathcal{F}^{-1} \left\{ \hat{\beta}(k) \mathcal{F}\left[\left(\frac{|B|}{B_0} \right)^r - 1 \right] \right\} H, \tag{B1}$$

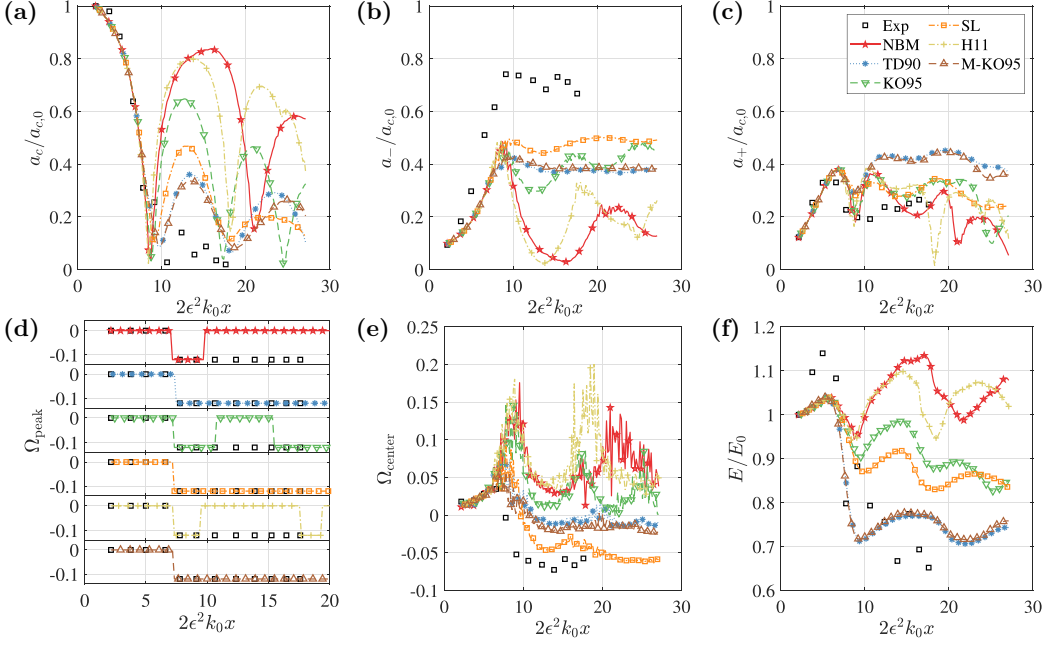where H is the Heaviside function corresponding to one of the three breaking criteria in Sec. V A.

FIG. 12. Similar to Figs. 3 and 11 but for case 3 from Table II.

Modified selective Laplacian model (M-SL)

In Fourier space, the modified selective Laplacian (M-SL) model can be written as

$$\hat{D} = \begin{cases} -\hat{\beta}(k)\frac{\omega_0}{k_0^2}(|k| - k^*)^2\hat{B}(k)H & \text{for } |k| > k^*, \\ 0 & \text{for } |k| \leqslant k^*, \end{cases} \tag{B2}$$

where $k^* = 1.2k_0$ as before.

Modified Hwung et al. (2011) model (M-H11)

The modified Hwung *et al.* (2011) (M-H11) model has the form

$$D = B\left(\frac{D_a}{g} + i4\gamma \int \frac{k_0 D_a}{g}\mathrm{d}x\right)H, \tag{B3}$$

where $D_a = \omega_0 k_0^2/2\mathcal{F}^{-1}(\hat{\beta}(k)\mathcal{F}(|B|^2))$.

Comparison between modified models

In Table IV we show the L2 loss for case 1, which is used in the optimization, and case 2 for the three modified models above. We find that model modification reduces the L2 loss in general. The fact that the L2 loss is not improved as much for case 2 as for case 1 suggests the modified model we proposed cannot generally explain both cases; the good agreement for case 1 may be due to overfitting. Among all the modified models, the M-KO95 model with a fixed-interval breaking criterion still achieves the lowest L2 loss for case 2 (not used for optimization).

In Fig. 14 we show the surface elevation profiles for the optimized models. Compared to the case with values of the parameters from the literature, only modest improvements in the agreement of the surface elevation of the breaking crests with experiments is obtained with the optimized parameters.
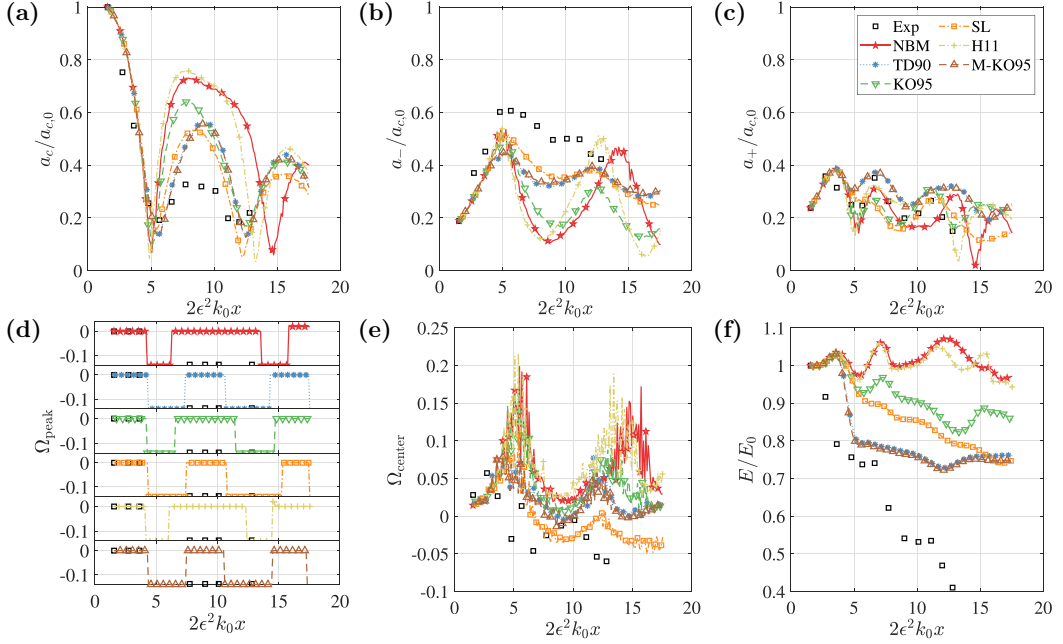
FIG. 13. Similar to Figs. 3 and 11 but for case 4 from Table II.

In Figs. 15 and 16 we examine the spectra for the optimized models and the modified models, respectively. Only the modified breaking models with a fixed-interval breaking criterion can reproduce the spectral dissipation of the "shoulder" correctly.

TABLE IV. Results from modification of the reduced-form breaking models (NBM denotes the case with no breaking model). The L2 loss is normalized by its value for the case with no breaking model.

Model	Breaking criterion	L2 loss (case 1)	L2 loss (case 2)
NBM	None	1.00	1.00
M-KO95	Geometric	0.68	0.90
M-KO95	Kinetic	0.52	0.92
M-KO95	Fixed interval	0.52	0.80
M-SL	Geometric	0.69	0.89
M-SL	Kinetic	0.56	0.89
M-SL	Fixed interval	0.65	0.88
M-H11	Geometric	0.97	1.00
M-H11	Kinetic	0.66	1.00
M-H11	Fixed interval	0.44	0.83
M-TD90	Geometric	0.65	0.91
M-TD90	Kinetic	0.33	0.92
M-TD90	Fixed interval	0.49	0.86

(a) TD90 model, Geometric   (b) KO95 model, Fixed Interval   (c) SL model, Fixed Interval   (d) H11 model, Kinematic
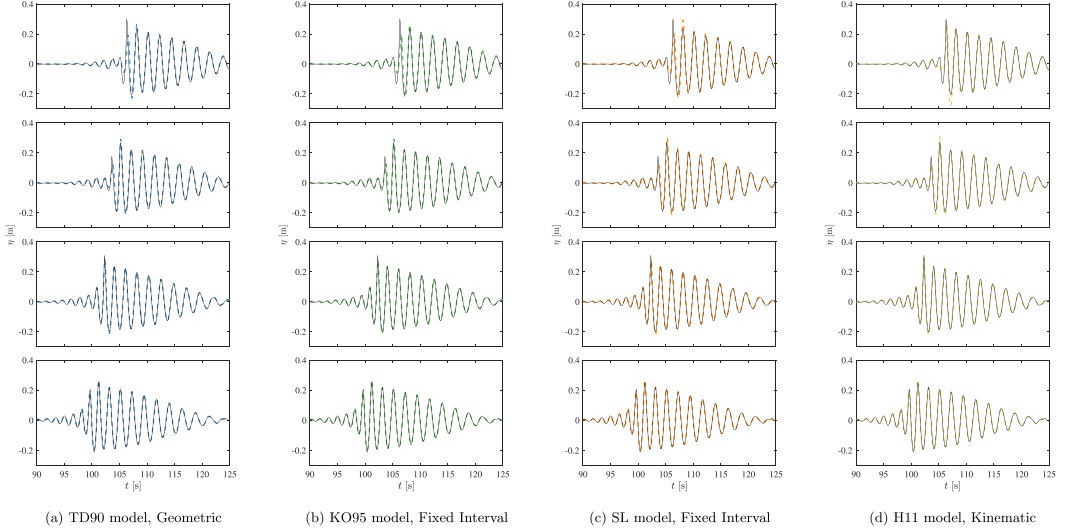
FIG. 14. For the reduced-form breaking models with optimized parameters, surface elevations at different gauge locations for focused wave groups (case 1 in Table I). Black solid lines correspond to experimental data and colored dashed lines to MNLS simulations with (a) the model of TD90; (b) the KO95 model with fixed-interval breaking criterion; (c) the SL model with fixed-interval breaking criterion; and (d) the H11 model with kinematic breaking criterion.

APPENDIX C: DISSIPATION ELEMENTS IN WATER TANK EXPERIMENTS

In this section we calculate the contribution from surface tension effect, internal friction, and bottom and sidewall friction one by one to show the dissipation in water tank experiments. In this paper two experiments are introduced. One is performed at Shanghai JiaoTong University (SJTU), and the other is performed at Aix-Marseille University (AMU), France. For the water tank experiment at SJTU, the wave tank was 300 m long, 16 m wide, with a water depth of 7.33 m. The frequency of carrier wave modeled is $f_0 = 0.5$ Hz. For the other water tank experiment performed at AMU, the wave tank was 40 m long, 2.7 m wide, with a water depth of 0.80 m. The highest carrier frequency of modulated plane-wave experiments is $f_0 = 1.6$ Hz.

Based on "rules of thumb" [32], we state that the surface tension contribution is negligible for both experiments as the wave period is greater than 0.35 s and water depth is larger than 2 cm. In our case the wave period is no less than 0.625 s and water depth is 0.8 m. Hence the surface tension is negligible for all cases in this study.

Keulegan [33] developed an expression to estimate the wave attenuation due to internal friction when boundary shear is negligible:

$$H(t) = H_0 e^{-8\pi \nu t/L^2}, \tag{C1}$$

where H_0 is the wave amplitude at $t = 0$ and H is the wave amplitude at a given time t. $\nu = 10^{-6}$ m^2/s is the kinematic viscosity of water and L is the wavelength. With (C1) we found that the height loss due to internal friction is 0.03% with propagation time $t = 155$ s for the SJTU experiment and 2.10% with propagation time $t = 100$ s for the AMU experiment.

Keulegan developed another formula to estimate the wave attenuation of a small amplitude linear wave in a wave flume with constant cross section [33]:

$$H_2/H_1 = e^{-\alpha x}, \tag{C2}$$

(a) Case 1, Before breaking ($x = 3.04$ m).

(b) Case 1, After breaking ($x = 6.50$ m).

(c) Case 2, Before breaking ($x = 3.04$ m).

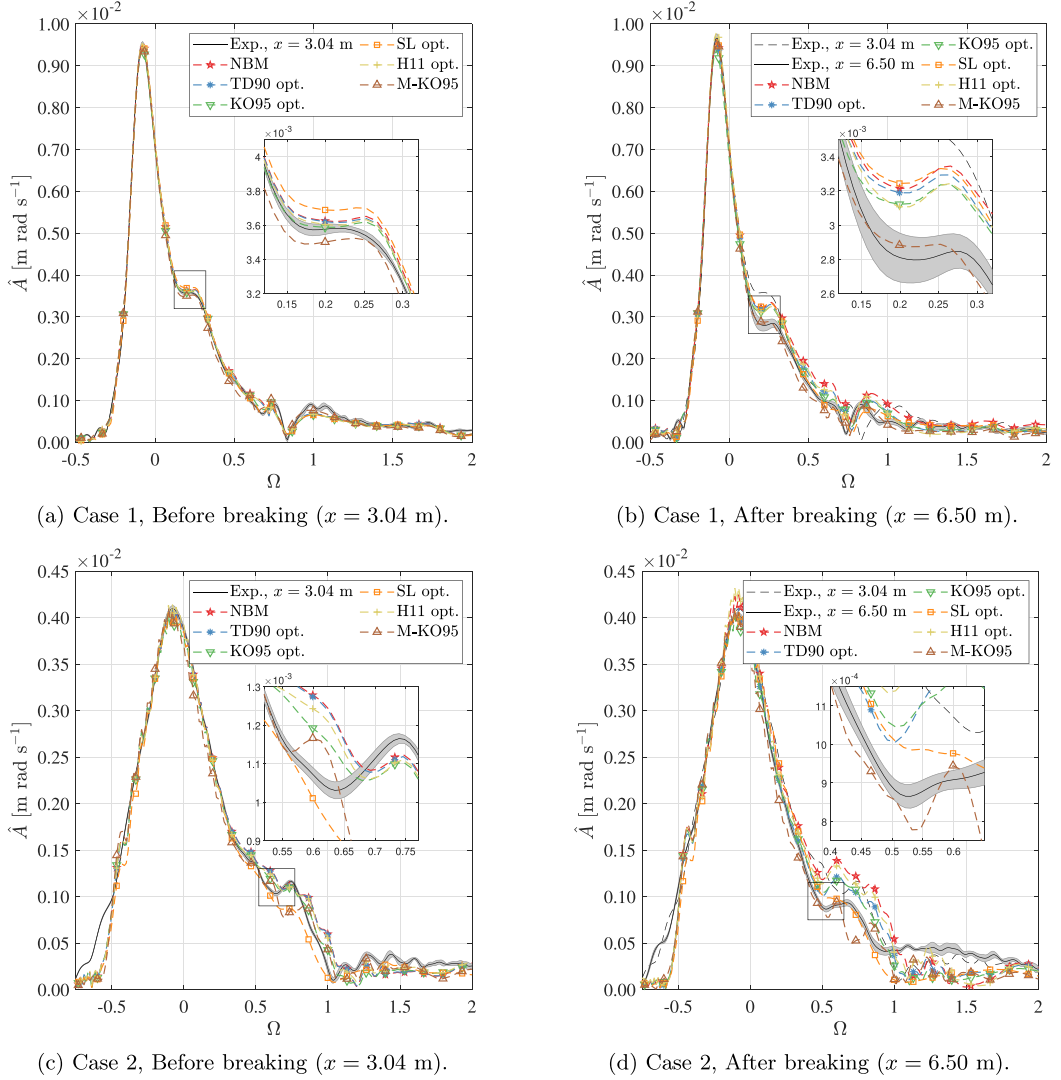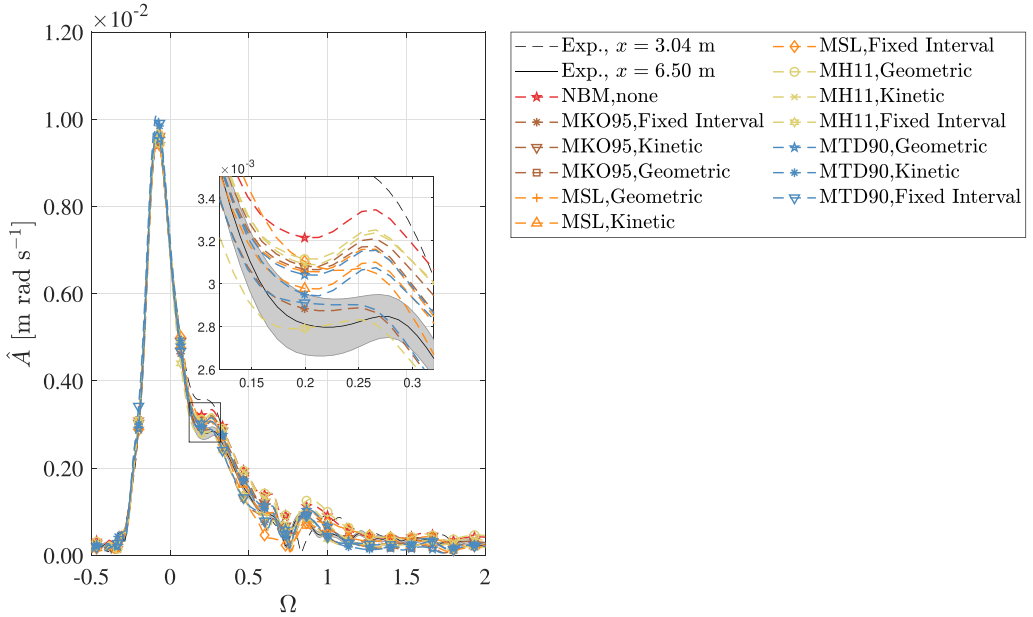(d) Case 2, After breaking ($x = 6.50$ m).

FIG. 15. For the case with optimized parameters, comparison of amplitude spectra before and after breaking of a focused wave group (case 1 and case 2 in Table I) for different reduced-form breaking models, including no breaking model (NBM), showing experiments (black solid/dashed lines), with gray shaded region corresponding to ± 1 standard deviation from repeated experiments, and MNLS simulations with different breaking models (colored dashed lines with markers).

where

$$\alpha = \frac{2}{BC}\sqrt{\frac{\pi \nu}{T}}\left[\frac{\sinh\left(\frac{4\pi h}{L}\right) + \frac{2\pi B}{L}}{\sinh\left(\frac{4\pi h}{L}\right) + \frac{4\pi h}{L}}\right], \tag{C3}$$

and H_1 is the wave height at $x = 0$ and H_2 is the wave height at a given propagation distance x. B is the tank width, T is the wave period, $C = L/T$ is the wave celerity, and h is the water depth. With (C2) we found that the height loss due to bottom and sidewall friction is 0.75% with propagation distance $x = 150$ m for the SJTU experiment and 6.58% with propagation distance $x = 40$ m for the AMU experiment.

(a) Case 1, After breaking ($x = 6.50$ m).
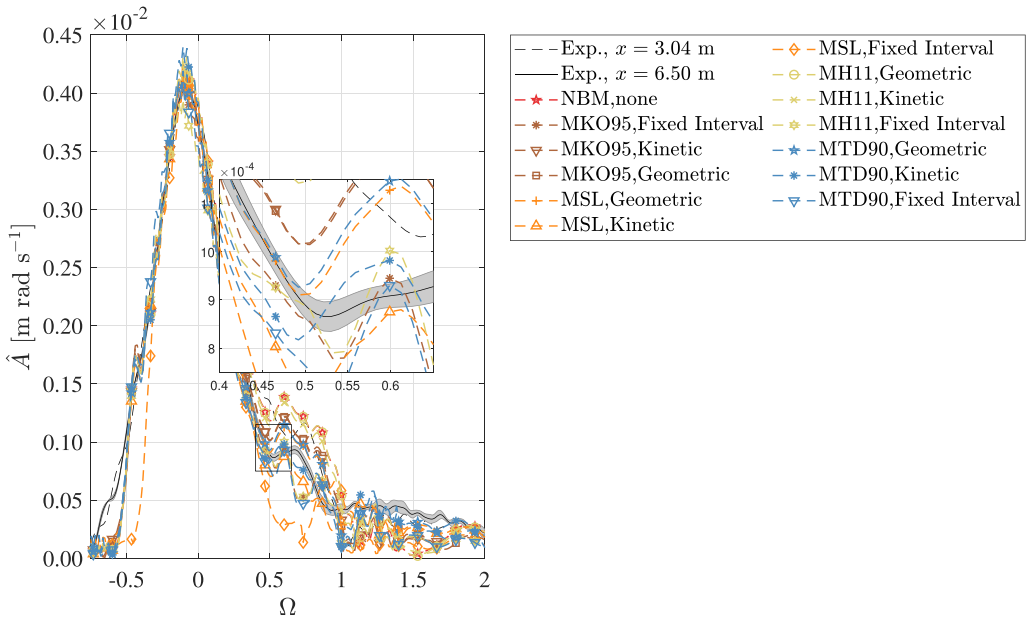
(b) Case 2, After breaking ($x = 6.50$ m).

FIG. 16. For the modified models, comparison of amplitude spectra after breaking of a focused wave group (case 1 and case 2 in Table I) for different modified reduced-form breaking models with different breaking criteria and the case with no breaking model (NBM), showing experiments (black solid/dashed lines), with gray shaded region corresponding to ± 1 standard deviation from repeated experiments, and MNLS simulations with different modified breaking models and breaking criteria (colored dashed lines with markers).

[1] A. Babanin, *Breaking and Dissipation of Ocean Surface Waves* (Cambridge University Press, Cambridge, United Kingdom, 2011).

[2] K. Hasselmann, On the spectral dissipation of ocean waves due to white capping, Boundary Layer Meteorol. **6**, 107 (1974).

[3] W. K. Melville, The role of surface-wave breaking in air-sea interaction, Annu. Rev. Fluid Mech. **28**, 279 (1996).

[4] L. Deike, Mass transfer at the ocean–atmosphere interface: The role of wave breaking, droplets, and bubbles, Annu. Rev. Fluid Mech. **54**, 191 (2022).

[5] A. Toffoli, A. Babanin, M. Onorato, and T. Waseda, Maximum steepness of oceanic waves: Field and laboratory experiments, Geophys. Res. Lett. **37**, 5 (2010).

[6] D. Peregrine, Water-wave impact on walls, Annu. Rev. Fluid Mech. **35**, 23 (2003).

[7] K. B. Dysthe, Note on a modification to the nonlinear Schrödinger equation for application to deep water waves, Proc. R. Soc. London, Ser. A. **369**, 105 (1979).

[8] K. B. Dysthe and K. Trulsen, The evolution of an evolution equation, Front. Nonlinear Phys. **2**, 125 (2001).

[9] T. A. A. Adcock and P. H. Taylor, Fast and local non-linear evolution of steep wave-groups on deep water: A comparison of approximate models to fully non-linear simulations, Phys. Fluids **28**, 016601 (2016).

[10] D. Eeltink, H. Branger, C. Luneau, Y. He, A. Chabchoub, J. Kasparian, T. S. van den Bremer, and T. P. Sapsis, Nonlinear wave evolution with data-driven breaking, Nat. Commun. **13**, 2343 (2022).

[11] K. Trulsen and K. B. Dysthe, *Frequency Down-Shift Through Self Modulation and Breaking* (Springer Netherlands, Dordrecht, 1990), pp. 561–572.

[12] Y. Kato and M. Oikawa, Wave number downshift in modulated wavetrain through a nonlinear damping effect, J. Phys. Soc. Jpn. **64**, 4660 (1995).

[13] A. Majda and X. Wang, The selective decay principle for barotropic geophysical flows, Methods Appl. Anal. **8**, 579 (2001).

[14] H. H. Hwung, W. S. Chiang, R. Y. Yang, and I. V. Shugan, Threshold model on the evolution of Stokes wave side-band instability, Eur. J. Mech. B Fluids **30**, 147 (2011).

[15] M. P. Tulin and T. Waseda, Laboratory observations of wave group evolution, including breaking effects, J. Fluid Mech. **378**, 197 (1999).

[16] T. B. Benjamin and J. E. Feir, The disintegration of wave trains on deep water, Part 1. Theory, J. Fluid Mech. **27**, 417 (1967).

[17] B. M. Lake, H. C. Yuen, H. Rungaldier, and W. E. Ferguson, Nonlinear deep-water waves: Theory and experiment, Part 2. Evolution of a continuous wave train, J. Fluid Mech. **83**, 49 (1977).

[18] E. Fermi, P. Pasta, S. Ulam, and M. Tsingou, Studies of the nonlinear problems, Technical Report, Report No. LA-1940, 1955.

[19] T. Dauxois, Fermi, Pasta, Ulam, and a mysterious lady, Phys. Today **61**(1), 55 (2008).

[20] W. K. Melville, The instability and breaking of deep-water waves, J. Fluid Mech. **115**, 165 (1982).

[21] W. Mostert, S. Popinet, and L. Deike, High-resolution direct simulation of deep water breaking waves: Transition to turbulence, bubbles and droplets production, J. Fluid Mech. **942**, A27 (2022).

[22] K. Trulsen, I. Kliakhandler, K. B. Dysthe, and M. G. Velarde, On weakly nonlinear modulation of waves on deep water, Phys. Fluids **12**, 2432 (2000).

[23] K. Trulsen and K. B. Dysthe, A modified nonlinear Schrödinger equation for broader bandwidth gravity waves on deep water, Wave Motion **24**, 281 (1996).

[24] A. Toffoli, O. Gramstad, K. Trulsen, J. Monbaliu, E. Bitner-Gregersen, and M. Onorato, Evolution of weakly nonlinear random directional waves: Laboratory experiments and numerical simulations, J. Fluid Mech. **664**, 313 (2010).

[25] J. R. Chaplin, On frequency-focusing unidirectional waves, Int. J. Offshore Polar Eng. **6**, 06 (1996).

[26] R. Gibson and C. Swan, The evolution of large ocean waves: The role of local and rapid spectral changes, Proc. R. Soc. A **463**, 21 (2007).

[27] T. A. A. Adcock and P. H. Taylor, Non-linear evolution of uni-directional focussed wave-groups on a deep water: A comparison of models, Appl. Ocean Res. **59**, 147 (2016).

[28] X. Barthelemy, M. L. Banner, W. L. Peirson, F. Fedele, M. Allis, and F. Dias, On a unified breaking onset threshold for gravity waves in deep and intermediate depth water, J. Fluid Mech. **841**, 463 (2018).

[29] J. D. Carter, C. W. Curtis, and H. Kalisch, Particle trajectories in nonlinear Schrödinger models, Water Waves **2**, 31 (2020).

[30] M. Derakhti, M. L. Banner, and J. T. Kirby, Predicting the breaking strength of gravity water waves in deep and intermediate depth, J. Fluid Mech. **848**, R2 (2018).

[31] R. Kurnia and E. van Groesen, High order Hamiltonian water wave models with wave-breaking mechanism, Coastal Eng. **93**, 55 (2014).

[32] B. Le Méhauté, *An Introduction to Water Waves* (Springer, Berlin, Heidelberg, 1976), pp. 197–211.

[33] G. H. Keulegan, Wave motion, in *Engineering Hydraulics* (John Wiley, New York, 1950), Chap. 11, p. 711.